Spatiotemporal imaging of 2D polariton wavepacket dynamics using free electrons

Yaniv Kurman[1,†], Raphael Dahan[1,†], Hanan Herzig Shenfux[2], Kangpeng Wang[1], Michael Yannai[1], Yuval Adiv[1], Ori Reinhardt[1], Luiz H. G. Tizei[3], Steffi Y. Woo[3], Jiahan Li[4], James H. Edgar[4], Mathieu Kociak[3], Frank H. L. Koppens[2,5*], and Ido Kaminer[1*]

[1]Department of Electrical Engineering, Technion, Israel Institute of Technology, 32000 Haifa, Israel

[2]ICFO-Institut de Ciències Fotòniques, The Barcelona Institute of Science and Technology, Av. Carl Friedrich Gauss 3, 08860 Castelldefels (Barcelona), Spain

[3]Laboratoire de Physique des Solides, Université Paris-Saclay, CNRS, 91405, Orsay, France

[4]Kansas State University, Tim Taylor Department of Chemical Engineering, Durland Hall, Manhattan, KS 66506 USA

[5]ICREA-Institució Catalana de Recerca i Estudis Avanats, Passeig Lluís Companys 23, 08010 Barcelona, Spain

[†]These authors contributed equally to the manuscript

*Correspondence to: kaminer@technion.ac.il , Frank.Koppens@icfo.eu

Coherent optical excitations in 2D materials, 2D polaritons, can generate a plethora of optical phenomena arising from the extraordinary dispersion relations that do not exist in regular materials. Probing of the dynamical phenomena of 2D polaritons require simultaneous spatial and temporal imaging capabilities and could reveal unknown coherent optical phenomena in 2D materials. Here we present a spatiotemporal measurement of 2D wavepacket dynamics, from its formation to its decay, using an ultrafast transmission electron microscope driven by femtosecond mid-infrared pulses. The ability to coherently-excite phonon-polariton wavepackets and probe their evolution in a non-destructive manner reveals intriguing dispersion-dependent dynamics that includes splitting of multi-branch wavepackets, and unexpectedly, wavepacket deceleration and acceleration. Having access to the full spatiotemporal dynamics of 2D wavepackets can be used to shed light on puzzles in topological polaritons and discover exotic nonlinear optical phenomena in 2D materials.

Understanding of the propagating optical polaritons in 2D materials has progressed from a promising concept (*1*) to a platform for demonstrating rich physical phenomena (*2*), now showing an impact on emerging opto-electronics (*3*) and nanophotonic technologies (4, 5). These polaritons exhibit relatively low loss and long propagation distances, simultaneous with extreme confinement factors (*6–8*), facilitating their light–matter interactions (9–*11*).

There is motivation to utilize the novel properties of 2D polaritons and integrate them into ultrafast optical technologies that rely on the spatiotemporal control of light. Conventional areas of ultrafast optics achieve such control using pulse-shaping (*12*) and dispersion engineering, which are instrumental, for example, in photonic waveguides (*13*). The attainment of similar control with 2D polaritons could promote the integration of 2D polaritonic materials in mature areas of science and technology and contribute to their fundamental understanding. However, the spatiotemporal control of 2D polariton wavepackets has remained out of reach for exactly the same reasons that make their potential applications exciting: they have extremely small wavelengths and are strongly confined inside the material. New capabilities are necessary for accessing the spatiotemporal dynamics of 2D polaritons and their wavepackets, with nanometric spatial resolution and femtosecond temporal resolution.

In this regard, it is particularly interesting to consider wavepackets in materials exhibiting hyperbolic dispersion (*14*, *15*): Polaritons in hyperbolic materials show rich physical behavior, ranging from negative refraction (*16*) and subdiffraction imaging (*14*) to effective Hawking radiation. While this has been seen in metamaterials, phonon polariton (PhP) excitations in 2D materials also exhibit hyperbolic dispersion (*8, 17*); the phononic resonance creates a dispersion relation that contains multiple branches (see Fig. 1B), which were shown to be tunable by the 2D material geometry, thickness, and surrounding environment (*4*, *5, 17*), reaching high confinement with relatively low losses, even in room temperature (*6*).

The peculiar dynamics of hyperbolic wavepackets can be seen by looking at the group velocity: the derivative of the dispersion, $\partial\omega/\partial k$, approaches zero in an hyperbolic medium, since the medium supports excitations with (in principle) arbitrarily large momenta. In practicality, the group velocity of PhPs is well defined, given an excitation of a finite bandwidth exciting a specific branch. However, in 2D hyperbolic materials, any coherent excitation is expected to simultaneously stimulate multiple PhP branches, each having different dynamics. Moreover, even a small variation in the excitation's bandwidth/frequency results in a large change of the polariton group velocity and the entire wavepacket propagation dynamics. These prospects are especially intriguing in 2D hyperbolic materials such as thin flakes of hexagonal boron nitride (hBN), where the group velocity of polaritons was shown be as low as c/500 over

a relatively wide bandwidth (*18*). To explore these prospects of hyperbolic wavepackets and reveal their novel physics, we need access to the field comprising the wavepacket during its evolution inside the 2D material.

Coherent wavepacket dynamics

Our approach to measure the spatiotemporal dynamics of hyperbolic PhP wavepackets inside isotopically pure hBN (^{11}B) flakes (*6*) is made possible by exploiting the interaction between free electrons and PhP wavepackets. The temporal dynamics is obtained using a pump-probe technique with a mid-infrared (IR) laser pump and a free electron probe in an ultrafast transmission electron microscope (UTEM) (*19–28*) (Fig. 1A). The pulsed free electron penetrates the sample and consequently changes its energy spectrum according to the integrated electric field along its path (inset of Fig. 1C). By energy filtering of the post-interaction electron, we can reconstruct the image of the PhP wavepacket. The use of laser-driven energy-filtered transmission electron microscopy (EFTEM) was first demonstrated in photon-induced nearfield electron microscopy (PINEM). Our approach takes PINEM to the mid-IR range and combines it with 2D materials, providing a test of dispersion models of 2D materials in the time domain.

We record the PhP wavepacket creation and propagation (Fig. 1D, and Movies S1 and S2 (*29*)), revealing rare physical behaviors, such as multi-branch wavepacket splitting, acceleration and deceleration. The measured acceleration and deceleration dynamics are especially surprising, as wavepackets conventionally have a fixed group velocity. In certain cases, as in the thin hyperbolic hBN flakes, the group velocity is expected to be very slow – indeed, we observed group velocities from c/45 to c/850 – and still, each wavepacket is expected to propagate with a fixed group velocity. In contrast with this expectation, we show that the dispersive nature of PhPs (i.e., their momenta change rapidly in frequency) facilitates acceleration and deceleration dynamics. This result serves as a key example for the rich physical phenomena that can be found when probing non-destructively the spatiotemporal dynamics of 2D polaritons using the unique combination of femtosecond temporal and nanometer spatial resolution of the UTEM.

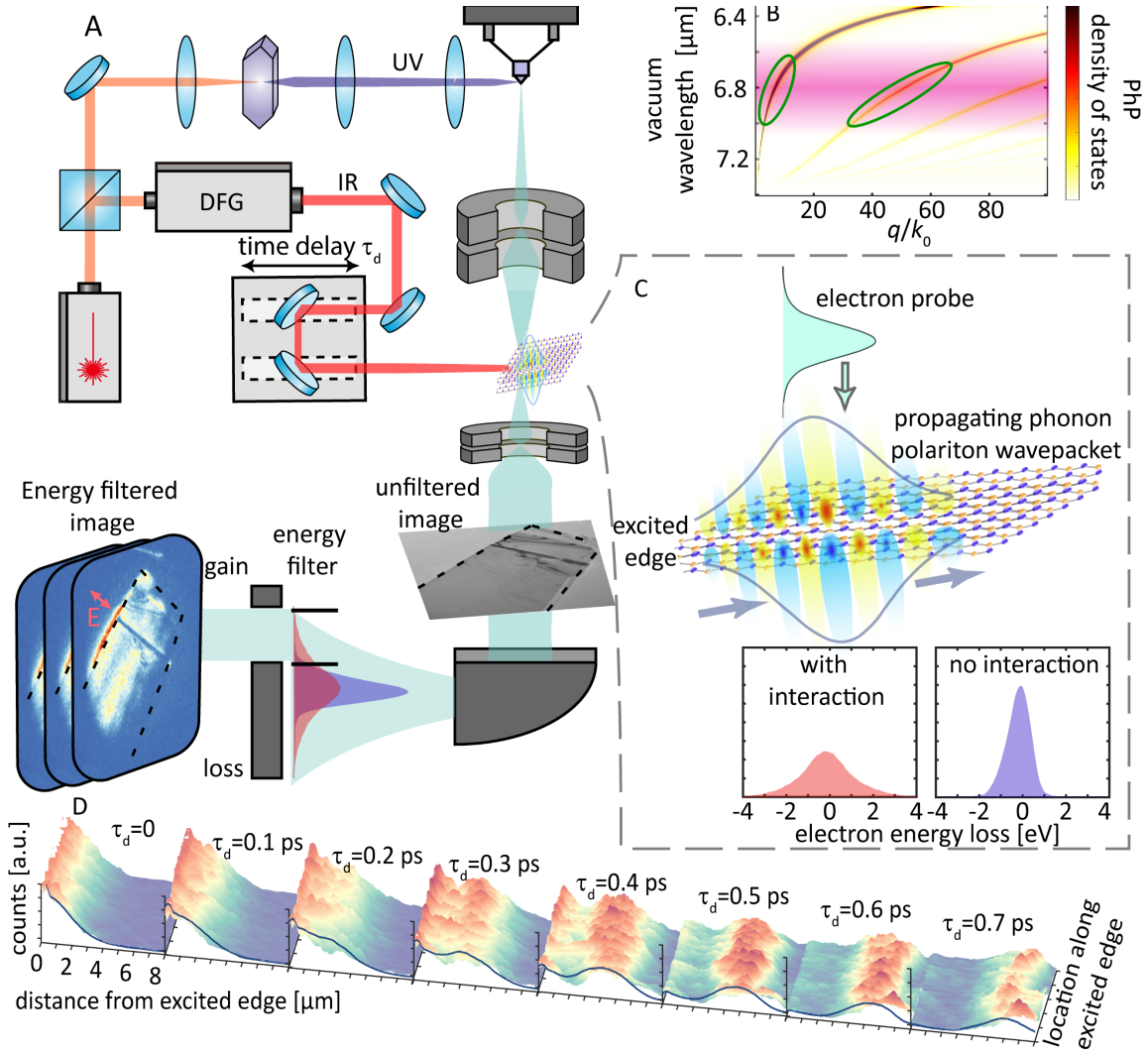

Fig. 1. Direct observation of 2D polariton wavepackets using ultrafast transmission electron microscopy (UTEM). (A) Experimental setup. A femtosecond laser (orange) splits into two branches. The bottom branch is converted into a mid-infrared (IR; red) pulse using difference frequency generation (DFG) and excites the phonon-polariton (PhP) wavepacket in the isotopically pure hBN (^{11}B) sample. The top branch is converted into an ultraviolet (UV; purple) pulse using fourth harmonic generation (FHG) and excites photo-electrically the electron pulse (cyan). The electron images the hBN sample when counting electrons at all energies (unfiltered image) and images the PhP wavepacket when counting only electrons that gained energy (filtered image). **(B)** Dispersion relation of a 55 nm thick isotopically pure hBN (^{11}B) flake on a 20 nm thick Si_3N_4 membrane (for sample-preparation (*29*)). The hyperbolic nature of hBN creates multiple dispersion branches in each frequency, each creating a different propagating wavepacket. The spectral bandwidth of the IR pulse (pink) excites a range of polariton modes (circled in green). **(C)** Free electron probing the (TM polarized) propagating PhP wavepacket inside the hBN. Insets: electron energy loss spectra (EELS) with the laser on (left) and off (right). **(D)** Measurement of the energy-filtered electrons for different time delays τ_d between the laser pulse and the electron probe, showing the propagation dynamics of the PhP wavepacket (shown in top-view in Fig. S1, and in Movie S1). Note that the definition of τ_d is up to arbitrary shifts in all figures and movies.

Imaging 2D polariton excitations

Among the various experimental techniques used in the field of 2D polaritons, scanning nearfield optical microscopy (SNOM) and its variants have had the most impact so far on the direct nearfield imaging of 2D polaritons (*6*, *17*, *30*). Recent advances in time-resolved SNOM also allowed the polariton's properties as group velocity to be extracted from the interference of scattered polaritons with different time delays (*18*, *31, 32*, *33*). However, this interferometric technique cannot image the wavepacket dynamics, as it does not provide the spectral phase, i.e., the phase difference between photons of different wavelengths. Other important experimental approaches, such as photo-emission electron microscopy (PEEM) (*34*), are also used for nearfield imaging in plasmonics; these approaches thus far did not access the mid- and far-IR region. We discuss the different experimental approaches in the Supplementary text (*29*). Importantly, techniques based on transmission electron microscopy stand out from all the above, since the electron penetrates through the sample and becomes sensitive also to the buried field rather than only to the field on the surface (*23*), an advantage for probing the highly confined 2D polaritons.

Our approach for the observation of PhP wavepacket dynamics adds to the toolbox of electron-beam spectroscopy and microscopy (*35*). Of particular importance for our approach are the advances in the imaging of polaritons using electron energy loss spectroscopy (EELS) (*36*), which reached the ability to measure IR excitations in vibrational electron spectroscopy (*37*). EELS enabled the measurement of purely vibrational modes (phonons) in bulk media and on surfaces (*38*) and the extraction of their dispersion relations using electron imaging and diffraction (*39*). In recent years, the improvements in the energy resolution of EELS (*37*), recently enabling the extraction of the PhP dispersion in extremely thin samples (*40*). Such experiments translated methodologies in electron microscopy, once applied to plasmons in the visible range (e.g., Refs. (*41*)), to phonons in the mid-IR range.

In all these EELS experiments, one obtains static, time-independent information on the polaritonic modes and other excitations of the sample, all of which are triggered by the free electron. In contrast, PINEM-based techniques such as ours use the electron only as a time-dependent probe (and not as a trigger of the excitation); thus, PINEM allows the extraction of time-dependent information on the temporal dynamics of the polaritons that are excited by a separate laser pulse.

Wavepacket creation and propagation

Fig. 1D and Movie S1 present an example of the measurements made of the wavepacket during its creation and propagation inside the flake. The video is created by repeating the measurement for a range of time delays between the laser pump and the electron probe. Such measurements of wavepacket dynamics rely on stimulated free-electron–PhP interactions. For the wavepacket, the electron is a non-destructive probe: the interaction alters the wavepacket in a negligible manner and hence does not interfere with the wavepacket evolution dynamics. Thus, the wavepacket propagates across the sample uninterrupted, starting from a single edge (chosen by optimizing the laser coupling (*29*)). At each time delay, the wavepacket profile is reconstructed from the electron energy distribution: at points where the PhP's out-of-plane electric field is stronger, there is a larger probability for the probing electron to gain energy and pass an energy filter. The energy filter is chosen to maximize the signal (see Fig. S4); it creates a threshold for the detectable PhP field and thus reduces the signal-to-noise ratio. Consequently, as we describe in the theory below, the connection between the number of counts and the electric field is non-linear.

To model the free-electron–PhP interaction, we find it essential to generalize the single-frequency theory of conventional PINEM (*20*, *21*) that was used to describe most PINEM experiments to date. The need to go beyond the successful PINEM theory lies in the finite bandwidth of the excitation laser (necessary for creating the pulsed PhP wavepacket) that excites the highly dispersive hBN PhPs. To capture the spectral bandwidth, we describe the free-electron–PhP coupling through a generalized coupling function $g(x,y,\omega)$. This coupling function g quantifies the strength of the interaction for each in-plane coordinate (x,y) and each frequency ω. According to this continuous-PINEM theory (*42*),

$$g(x,y,\omega)=\frac{e}{\hbar\omega}\int_{-\infty}^{\infty}dz\,E_z(x,y,z,\omega)e^{-i\frac{\omega}{v}z}, \tag{1}$$

where e and v are the electron charge and velocity, respectively, and $\hbar$ is the reduced Planck's constant. The integral is performed along the electron propagation direction z, on the z component of the electric field phasor $E_z(\omega)=\int E_z(t)e^{i\omega t}dt$, which includes all the PhPs modes due to their TM polarization.

The PhP wavepacket is imprinted on the electron as a time-dependent phase modulation:

$$\exp\left(2i\int_0^{\infty}d\omega\,|g(x,y,\omega)|\sin\big(\omega t-\arg\big(g(x,y,\omega)\big)\big)\right). \tag{2}$$

This phase modulation multiplies the initial electron wavefunction with a time delay (τ_d) relative to the PhP wavepacket excitation; τ_d is shifted for recording a video of the dynamics. Our theory predicts the measured electron energy spectra as the Fourier transform (time→energy) of the resulting electron wavefunction. Eq. (2) shows how larger g values imply stronger modulation in the phase of the free-electron wavefunction, equivalent to the electron gaining and losing more energy (*29*). The energy required for a detectable signal is related to the incoherent energy width of the pre-interaction electron (also called zero-loss peak). Because the width (0.9 eV in our system, Fig. 1C, right inset) is larger than the energy of a single PhP quanta, the post-interaction EELS (Fig. 1C, left inset) does not have discrete peaks as in PINEM experiments in the visible or near-IR range (*26*). Nevertheless, the change in the electron's energy is sufficient for probing the PhP wavepacket: the electron image in the *x-y* plane is filtered by energy for different time delays τ_d to extract the PhP spatiotemporal dynamics.

In the analysis of the measured PhP wavepacket dynamics, we first extract the field profile along the direction of propagation (Fig. 2A). When averaging the signal along the sample's excited edge, we reduce the signal-to-noise ratio (described in (*29*)). We find that a combination of a Gaussian and an exponential decay due to the edge effect provide together a good fit to the measured wavepacket, which can also capture the slowly moving higher branches quite accurately. This analysis reveals the formation of the wavepacket during the arrival of the excitation pulse. Fig. 2B shows an intriguing phenomenon: the wavepacket appears to remain stuck at the edge for a certain time duration and does not immediately propagate away from the boundary. Instead, the wavepacket's width and amplitude gradually increase. Thus, the gradually forming wavepacket increases in amplitude while remaining near the edge. Only toward the end of the excitation pulse (when its tail arrives) does the wavepacket start to move away from the edge more quickly, exhibiting phenomena of acceleration and deceleration that vary between samples and excitation wavelengths. Once the excitation pulse is ended, we can extract the stable group velocities.

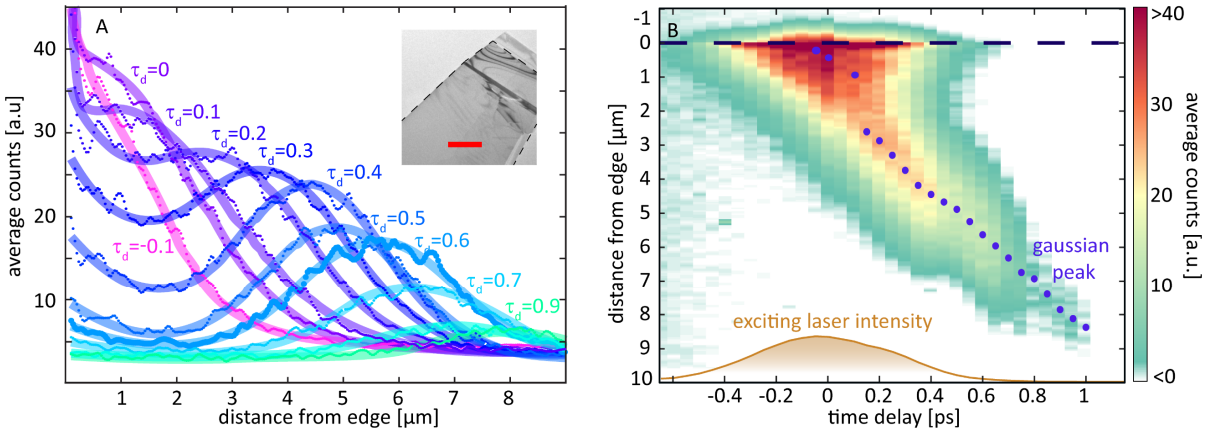

Fig. 2. Direct observation of the phonon-polariton (PhP) wavepacket's spatiotemporal dynamics. (A) Measured signal when averaged along the edge direction (dots) with the fit of a Gaussian profile plus an exponential decay for each measurement (blue-green curves). The times are in units of ps. Inset: unfiltered image of the hBN flake; the scale bar denotes 5 μm. **(B)** Map presenting the measured wavepacket as a function of time and distance from the edge; the blue dots represent the Gaussian wavepacket peak and gold the laser excitation intensity. At short times, while the laser is still on, the group velocity undergoes changes. In this figure, the time delay $\tau_d = 0$ is related to the peak of the excitation intensity. This measurement uses a 55 nm thick hBN flake, excited by a 6470 nm laser with a bandwidth of 175 nm.

The wavepacket properties during its formation, propagation, and gradual decay are summarized for three different samples and a range of excitation pulses (Figs. 3A-C). As expected, the group velocities become smaller as the sample thickness decreases. The lowest measured group velocity (bright blue in A) is 0.35 μm/ps, which is 860 times lower than the speed of light in vacuum. In a thicker sample, the fastest recorded group velocity is 6.7 μm/ps, which is 45 times lower than the speed of light in vacuum, but still sufficiently low for our free-electron probing technique to record the dynamics. An additional measurement includes the propagation over a duration of more than 2.5 ps in a 7.5 nm thick sample and propagation lengths over distances of more than 12 μm for a 55 nm thick sample, crossing the entire length of the sample. These propagation distances and durations are a merit of the isotopically pure hBN (^{11}B), which encounters smaller losses than normal hBN flakes (*6*).

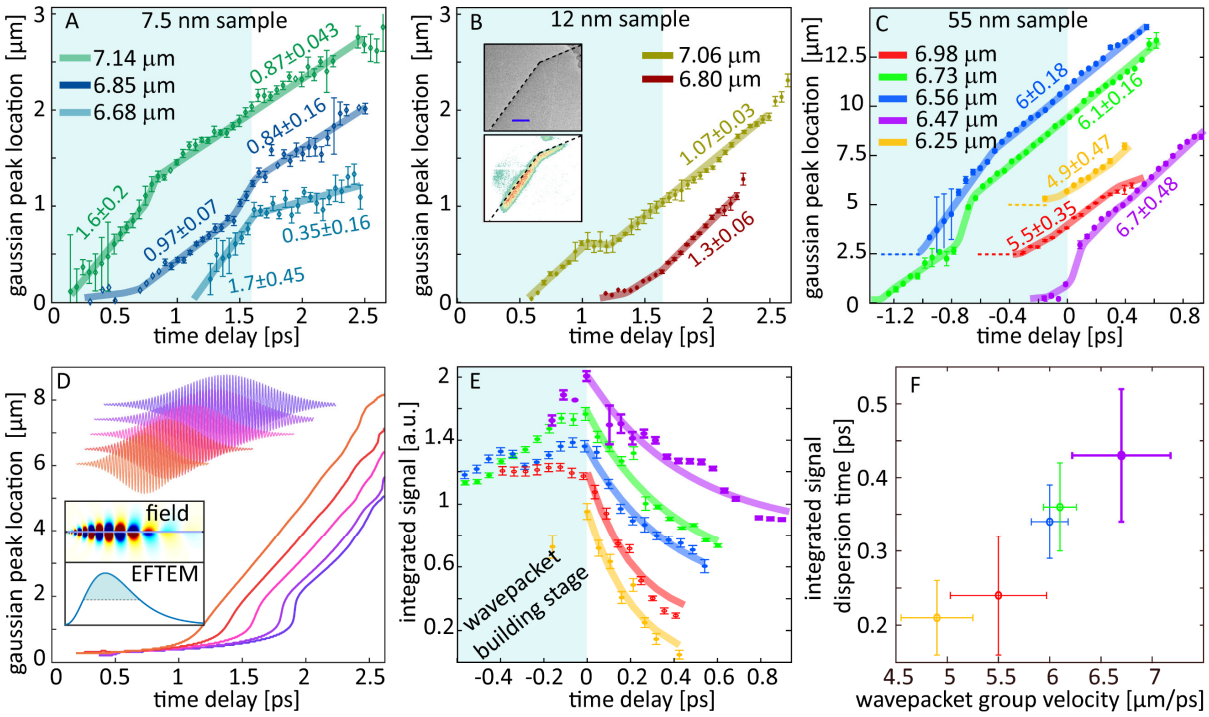

Fig. 3. Analysis of the PhP wavepacket formation, propagation, and decay - extracting the group velocities and wavepacket behavior. (A-C) The fitted Gaussian peak locations as a function of time with the extracted group velocities in units of µm/ps. We compare three $h^{11}BN$ samples having a thickness of **(A)** 7.5 nm, **(B)** 12 nm, and **(C)** 55 nm. For a better visualization, each measurement is shifted in time to a fixed end-time of the pumping (colored background) and shifted in space (by 0, 2.5, or 5 μm) as marked by dashed horizontal lines in (C). See Table S1 for excitation profiles. Top inset in (B): unfiltered image of the 12 nm sample (dashed lines represent sample edges); scale bar is 5 μm. Bottom inset in (B): an electron energy loss filtered image showing the group at a specific time. **(D)** Simulation results of the wavepacket peak location as a function of time in a 55 nm $h^{11}BN$ sample on a 20 nm Si_3N_4 membrane, comparing different levels of chirp (the excitations' temporal profiles are brought above the curves). The simulations show the acceleration and deceleration observed experimentally. Top inset: the simulated field. Bottom inset: the energy-filtered electron signal calculated using the field from the top inset, showing that the PINEM technique indeed extracts the wavepacket profile. Further simulations of the velocity change can be seen in Fig. S5 and movies S3 and S4. **(E)** Wavepacket integrated signal (derivation in (*29*), which helps identify the transition from a formation stage, in which the pump overcomes the dispersion and intrinsic PhP Ohmic losses, to the eventual decay (the effective timescales are denoted in ps). **(F)** There is a clear correlation between the dispersion rate and the wavepacket's group velocity, as expected by theory: wavepackets with higher group velocities are less dispersive.

The data show a first demonstration of a change in the group velocities of PhP wavepackets during their propagation, for which we use the terminology wavepacket acceleration and deceleration. We observed this effect in all sample thicknesses (Fig. 3(A-C)). For example, in the 7.5 nm sample, the group velocity decreased by a factor of 5 (Fig. 3(A)).

This effect is surprising, because the PhP dispersion is expected to cause the slower modes to decay faster, which would result in acceleration rather than deceleration.

We find that this effect reveals a more general S-shaped trajectory for the PhP wavepackets: during the pulse excitation (bright colored background in the panels of Fig. 3), the wavepacket first remains near the edge of the sample (extraordinarily slow group velocity), then experiences fast propagation, and finally decelerates to reach its final steady propagation velocity. The first two regimes are related to the excitation pulse duration and chirp, which pumps the PhP with different spectral components at different times. The measured phenomena of wavepacket deceleration and acceleration are consistent with the continuous-PINEM analysis of a set of finite-difference time-domain (FDTD) simulations, as shown in Fig. 3D, Fig. S5, and Movies S3 and S4. The simulations show that when the pulse is longer, and/or when the chirp is stronger, the change in velocity becomes more dominant, in agreement with our measurements.

Analysis of wavepacket dynamics

Our experiment identifies intriguing features of the PhP wavepackets during the wavepacket formation and free propagation. We integrate over the entire observable signal at each time delay to analyze the competition between the laser pumping to the dispersion and decay. We identify two features in the PhP wavepacket dynamics: First is the gradual buildup of the wavepacket when the pump overcomes the PhP wavepacket dispersion and intrinsic Ohmic losses (shown as bright background in Fig. 3E). We identify cases for which the integrated signal continues to grow even when the wavepacket peak is already 10 μm from the edge and is propagating at a stable group velocity (green curves). Secondly, the measured wavepackets disperse and decay at different rates (Fig. 3E-F), quantified by a dispersion time τ (Fig. 3E). The dispersion causes wavepacket broadening that reduces the field amplitude and thus also reduces the detected electron signal. The detected electron signal also varies with frequency, because different PhP modes have different confinements (see (*29*) for a quantitative analysis of the signal dependence on PhP confinement). As a result, the decay in the integrated signal is caused mostly by the wavepacket dispersion (sub-ps timescale) and not by intrinsic Ohmic loss (few ps timescale). As expected from theory, shorter dispersion times (i.e., larger dispersion) occur for slower group velocities.

The efficient PINEM interaction enables measurement of the propagation of multi-branch wavepackets that split over time into distinguishable Gaussian-like wavepackets of

different group velocities (Fig. 4 and Movie S2). The multi-branch wavepackets are created because the excitation at each wavelength can couple into more than a single branch in the dispersion relations (Fig. 1B), a phenomenon which was also observed in plasmonic structures (*34*). Fig. 4A shows the propagation of a multi-branch PhP wavepacket that splits into two single-branch wavepackets, propagating as a double Gaussian (Fig. 4B). From the location of the double Gaussian peaks (shown in Fig. 4C), we extract two different group velocities for the first- and second-branch wavepackets (6 and 1.1 μm/ps, respectively). We enhanced the observation of this effect by changing the electron energy slit to be sensitive to a smaller threshold electric field. As confirmed by the FDTD simulations (Fig. 4D-G), at short times the two wavepackets completely overlap. Then, at longer times the wavepackets gradually split from one another. Interestingly, as also confirmed by the FDTD simulation, the PINEM-type measurement shows a clear spatial separation between the wavepackets while their fields still appear to overlap. It is the electron's sensitivity to the field inside the hBN that enables one to distinguish the individual profiles of the two partially-overlapping wavepackets.

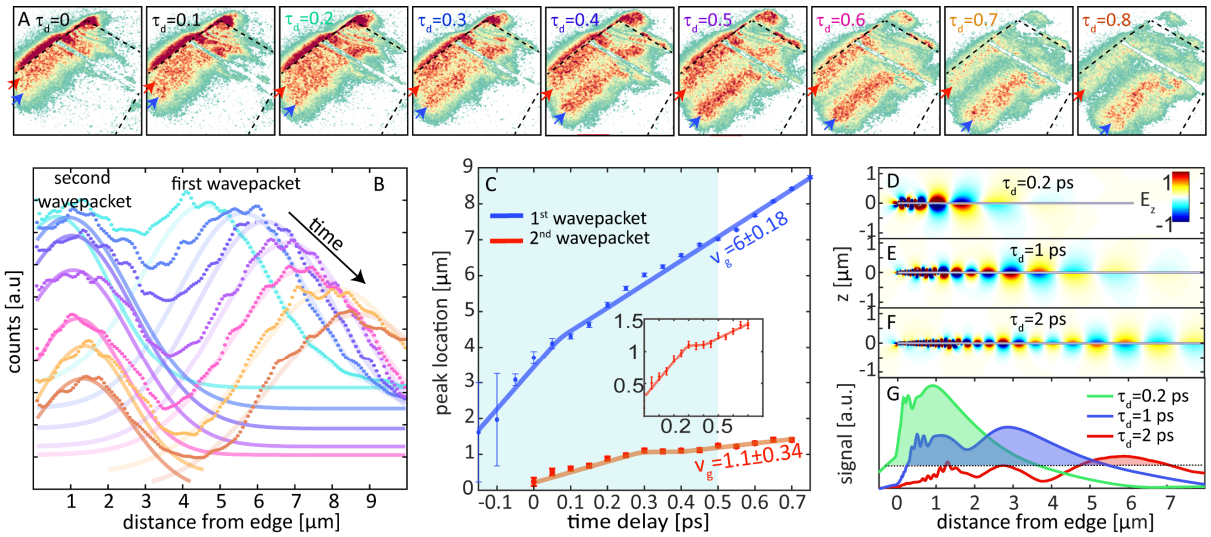

Figure 4: Observation of a multi-branch PhP wavepacket that splits into two distinct wavepackets of different branches and different group velocities. (A) Snapshots at different times of the two wavepackets propagating through the sample, with small blue and red arrows marking the peaks of each wavepacket. **(B)** Measured signal when averaged along the edge (dotted curves) with the double-Gaussian fit for each measurement (solid curves). The data show two distinct wavepackets with different group velocities. The time steps between the curves are 0.1 ps, starting at $\tau_d = 0.2$ ps. **(C)** Locations of the two wavepackets as a function of time, extracting the group velocities in units of μm/ps. The colored background represents times at which the wavepacket is still being pumped, as the excitation pulse has not ended. Inset: zoom-in on the 2nd wavepacket trajectory. **(D-F)** Simulated z-component of the electric field of a 55 nm hBN flake on a 20 nm thick Si_3N_4 membrane at specific times τ_d, showing an example of wavepacket evolution as it splits into multiple individual wavepackets of different orders. **(G)** The electron energy-filtered signal, calculated using the fields from (D-F) and thus

extracting the wavepacket profiles above a certain cutoff (shaded area). The signal shows a clear distinction between the wavepacket of the first mode and the second mode, similar to the experimental results.

We found that the PINEM interaction remains efficient for polariton wavepackets at higher-order branches. This feature is seen in the experimental data: the first- and second-order PhP branches provide a signal of a similar magnitude (Fig. 4B). Our numerical simulations confirmed this result: despite the second-branch having an overall smaller energy (due to less efficient coupling), the PINEM signal is of comparable strength. This result arises from the nature of the interaction, whereby the electron integrates along its trajectory and thus includes the field inside the hBN, which is larger as the field is more confined. Higher-branch modes have larger confinement and thus higher field amplitudes and yet they decay faster along the *z* direction; thus, the integrated signal remains comparable. Most nearfield imaging techniques probe the surface of the material and are thus essentially less efficient when the goal is to image wavepackets in higher-order branches, since they decay more rapidly along the *z* direction (the inefficient light out-coupling of the higher-branches reduces the signal further). By using the penetration of free electrons, PINEM-type techniques such as ours bypass these limits, becoming especially advantageous for imaging higher-branch polaritonic modes and highly confined polaritons in general.

Concluding remarks and Outlook

The measured phenomena are fully captured by the linear optical response of hyperbolic media, as verified by our simulations. Finding the nonlinear optical response of hBN is still a topic of ongoing investigation (*43*, *44*) and should require stronger fields compared to the values in our experiments (electric field of ~1.5 MV/m (*29*)). Future investigation of optical nonlinearities in 2D materials has prospects for the observation of spatiotemporal soliton-wavepackets of 2D polaritons and novel forms of 2D shockwaves and light bullets.

Our work builds on key advances in the areas of PINEM, ultrafast electron microscopy, and ultrafast electron diffraction (*25*). Whereas PINEM techniques have examined the temporal dynamics of optical excitations by interference patterns of plasmon polaritons (*26*) and decay of photonic cavity modes (*27*, *28*), our experiments resolve the dynamics of the entire optical wavepacket due to the slower group velocities and shorter wavepacket extents of PhPs. The slow group velocity causes the wavepacket envelope to remain almost static within the duration of the electron interaction (the wavepacket moves only a fraction of a micron during the

electron's duration, 0.13 ps standard deviation); thus, we can record the wavepacket dynamics. In this manner, our experiment is operated at frequencies that are in between the optical range and the range of mechanical vibrations (typically at GHz frequencies), where the dynamics of phonons was observed thanks to their slow oscillation relative to the duration of the electron probe (*22*, *24*). The PhPs in our experiment differ from these mechanical vibrations by being coherent optical excitations, which are in fact hybrids of the mechanical vibrations (optical phonons) and photons in the IR region. Consequently, the imaging of polaritons in 2D materials utilize advantages from both plasmon imaging (*26*) and phonon imaging (*22*, *24*).

References and Notes

1. M. Jablan, H. Buljan, M. Soljacic, Plasmonics in graphene at infrared frequencies. *Phys. Rev. B* **80**, 1–7 (2009).
2. D. N. Basov, A. Asenjo-Garcia, P. J. Schuck, X. Zhu, A. Rubio, Polariton panorama. *Nanophotonics* **10**, 549–577 (2020).
3. V. W. Brar, M. C. Sherrott, D. Jariwala, Emerging photonic architectures in two-dimensional opto-electronics. *Chem. Soc. Rev.* **47**, 6824–6844 (2018).
4. P. Li *et al.* Hyperbolic phonon-polaritons in boron nitride for near-field optical imaging and focusing. *Nat. Commun.* **6**, 1–9 (2015).
5. K. Chaudhary *et al.* Engineering phonon polaritons in van der Waals heterostructures to enhance in-plane optical anisotropy. *Sci. Adv.* **5**, eaau7171 (2019).
6. A. J. Giles *et al.* Ultralow-loss polaritons in isotopically pure boron nitride. *Nat. Mater.* **17**, 134–139 (2018).
7. D. Alcaraz Iranzo *et al.* Probing the ultimate plasmon confinement limits with a van der Waals heterostructure. *Science*. **360**, 291–295 (2018).
8. W. Ma *et al.* In-plane anisotropic and ultra-low-loss polaritons in a natural van der Waals crystal. *Nature*. **562**, 557–562 (2018).
9. Y. Kurman, I. Kaminer, Tunable bandgap renormalization by nonlocal ultra-strong coupling in nanophotonics. *Nat. Phys.* **16**, 868–874 (2020).
10. N. Rivera, I. Kaminer, Light–matter interactions with photonic quasiparticles. *Nat. Rev. Phys.* **2**, 538–561 (2020).
11. I. Epstein *et al.* Far-field excitation of single graphene plasmon cavities with ultracompressed mode volumes. *Science*. **368**, 1219–1223 (2020).
12. A. M. Weiner, Femtosecond pulse shaping using spatial light modulators. *Rev. Sci. Instrum.* **71**, 1929–1960 (2000).
13. P. Colman *et al.* Temporal solitons and pulse compression in photonic crystal waveguides. *Nat. Photonics.* **4**, 862–868 (2010).
14. M. A. Noginov *et al.* Bulk photonic metamaterial with hyperbolic dispersion. *Appl. Phys. Lett.* **94**, 1–4 (2009).
15. A. Poddubny, I. Iorsh, P. Belov, Y. Kivshar, Hyperbolic metamaterials. *Nat. Photonics*. **7**, 958–967 (2013).
16. K. V. Sreekanth, A. De Luca, G. Strangi, Negative refraction in graphene-based hyperbolic metamaterials. *Appl. Phys. Lett.* **103**, 023107 (2013).
17. S. Dai *et al.* Tunable Phonon Polaritons in Atomically Thin van der Waals Crystals of Boron Nitride. *Science*. **343**, 1125–1129 (2014).
18. E. Yoxall *et al.* Direct observation of ultraslow hyperbolic polariton propagation with negative phase velocity. *Nat. Photonics*. **9**, 674–678 (2015).
19. B. Barwick, D. J. Flannigan, A. H. Zewail, Photon-induced near-field electron microscopy. Nature. 462, 902–906 (2009).
20. F. J. Garcia De Abajo, A. Asenjo-Garcia, M. Kociak, Multiphoton absorption and emission by interaction of swift electrons with evanescent light fields. *Nano Lett.* **10**, 1859–1863 (2010).
21. S. T. Park, M. Lin, A. H. Zewail, Photon-induced near-field electron microscopy (PINEM): theoretical and experimental. *New J. Phys.* **12**, 123028 (2010).

22. D. T. Valley, V. E. Ferry, D. J. Flannigan, Imaging Intra- and Interparticle Acousto-plasmonic Vibrational Dynamics with Ultrafast Electron Microscopy. *Nano Lett.* **16**, 7302–7308 (2016).
23. T. T. A. Lummen *et al.* Imaging and controlling plasmonic interference fields at buried interfaces. *Nat. Commun.* **7**, 1–9 (2016).
24. D. R. Cremons, D. A. Plemmons, D. J. Flannigan, Femtosecond electron imaging of defect-modulated phonon dynamics. *Nat. Commun.* **7**, 11230 (2016).
25. Y. Morimoto, P. Baum, Diffraction and microscopy with attosecond electron pulse trains. *Nat. Phys.* **14**, 252–256 (2018).
26. I. Madan *et al.* Holographic imaging of electromagnetic fields via electron-light quantum interference. *Sci. Adv*. **5**, aav8358 (2019).
27. K. Wang *et al.* Coherent interaction between free electrons and a photonic cavity. *Nature*. **582**, 50–54 (2020).
28. O. Kfir *et al.* Controlling free electrons with optical whispering-gallery modes. *Nature*. **582**, 46–49 (2020).
29. See supplementary materials.
30. R. Hillenbrand, T. Taubner, F. Keilmann, Phonon-enhanced light–matter interaction at the nanometre scale. *Nature*. **418**, 159–162 (2002).
31. M. A. Huber *et al.* Femtosecond photo-switching of interface polaritons in black phosphorus heterostructures. *Nat. Nanotechnol*. **12**, 207–211 (2017).
32. M. Mrejen, L. Yadgarov, A. Levanon, H. Suchowski, Transient exciton-polariton dynamics in WSe2 by ultrafast near-field imaging. *Sci. Adv.* **5**, aat9618 (2019).
33. A. J. Sternbach *et al.* Programmable hyperbolic polaritons in van der Waals semiconductors. *Science* **371**, 617–620 (2021).
34. B. Frank *et al.* Short-range surface plasmonics: Localized electron emission dynamics from a 60-nm spot on an atomically flat single-crystalline gold surface. *Sci. Adv.* **3**, e1700721 (2017).
35. A. Polman, M. Kociak, F. J. García de Abajo, Electron-beam spectroscopy for nanophotonics. Nat. Mater. 18, 1158–1171 (2019).
36. R. F. Egerton, *Electron Energy-Loss Spectroscopy in the Electron Microscope* (Springer US, Boston, MA, 2011).
37. O. L. Krivanek *et al.* Vibrational spectroscopy in the electron microscope. *Nature*. **514**, 209–212 (2014).
38. X. Li *et al.* Three-dimensional vectorial imaging of surface phonon polaritons. *Science*. **371**, 1364–1367 (2021).
39. F. S. Hage *et al.* Nanoscale momentum-resolved vibrational spectroscopy. *Sci. Adv*. **4**, eaar7495 (2018).
40. N. Li *et al.* Direct observation of highly confined phonon polaritons in suspended monolayer hexagonal boron nitride. *Nat. Mater*. **20**, 43–48 (2021).
41. J. Nelayah *et al.* Mapping surface plasmons on a single metallic nanoparticle. *Nat. Phys.* **3**, 348–353 (2007).
42. O. Reinhardt, I. Kaminer, Theory of Shaping Electron Wavepackets with Light. *ACS Photonics*. **7**, 2859–2870 (2020).
43. M. Mehdi Jadidi *et al.* Phonon-polariton-enhanced nonlinearity in hexagonal boron nitride. *Conference on Lasers and Electro-Optics*, paper FTh4A.6 (OSA, 2020).
44. A. A. Popkova *et al.* Optical Third-Harmonic Generation in Hexagonal Boron Nitride Thin Films. *ACS Photonics.* **8**, 824–831 (2021).
45. G. M. Vanacore, I. Madan, G. Berruto, K. Wang, E. Pomarico, R. J. Lamb, D. McGrouther, I. Kaminer, B. Barwick, F. J. García De Abajo, F. Carbone, Attosecond coherent control of free-electron wave functions using semi-infinite light fields. *Nat. Commun.* **9**, 2694 (2018).
46. A. A. Lanin, A. A. Voronin, A. B. Fedotov, A. M. Zheltikov, Time-domain spectroscopy in the mid-infrared. *Sci. Rep.* **4**, 6670 (2015).
47. Y. Wu, J. Ordonez-Miranda, S. Gluchko, R. Anufriev, D. de Sousa Meneses, L. Del Campo, S. Volz, M. Nomura, Enhanced thermal conduction by surface phonon-polaritons. *Sci. Adv.* **6**, aebb4461 (2020).
48. S. Liu, R. He, L. Xue, J. Li, B. Liu, J. H. Edgar, Single Crystal Growth of Millimeter-Sized Monoisotopic Hexagonal Boron Nitride. *Chem. Mater.* **30**, 6222–6225 (2018).
49. T. Malis, S. C. Cheng, R. F. Egerton, EELS log-ratio technique for specimen-thickness measurement in the TEM. *J. Electron Microsc. Tech.* **8**, 193–200 (1988).
50. H. Shinotsuka, S. Tanuma, C. J. Powell, D. R. Penn, Calculations of electron inelastic mean free paths . XII . Data for the full Penn algorithm . **51**, 427–457 (2018).
51. A. Castellanos-Gomez, M. Buscema, R. Molenaar, V. Singh, L. Janssen, H. S. J. van der Zant, G. A. Steele, Deterministic transfer of two-dimensional materials by all-dry viscoelastic stamping. *2D Mater.* **1**,

011002 (2014).
52. R. Frisenda, E. Navarro-Moratalla, P. Gant, D. Pérez De Lara, P. Jarillo-Herrero, R. V. Gorbachev, A. Castellanos-Gomez, Recent progress in the assembly of nanodevices and van der Waals heterostructures by deterministic placement of 2D materials. *Chem. Soc. Rev.* **47**, 53–68 (2018).
53. E. J. C. Dias, F. J. García De Abajo, Fundamental Limits to the Coupling between Light and 2D Polaritons by Small Scatterers. *ACS Nano*. **13**, 5184–5197 (2019).
54. N. Talebi, *Near-Field-Mediated Photon–Electron Interactions* (Springer International Publishing, Cham, 2019).
55. K. E. Priebe, C. Rathje, S. V. Yalunin, T. Hohage, A. Feist, S. Schäfer, C. Ropers, Attosecond electron pulse trains and quantum state reconstruction in ultrafast transmission electron microscopy. *Nat. Photonics*. **11**, 793–797 (2017).
56. M. L. M. Balistreri, H. Gersen, J. P. Korterik, L. Kuipers, N. F. Van Hulst, Tracking femtosecond laser pulses in space and time. *Science.* **294**, 1080–1082 (2001).
57. Y. Gong, A. G. Joly, D. Hu, P. Z. El-Khoury, W. P. Hess, Ultrafast imaging of surface plasmons propagating on a gold surface. *Nano Lett.* **15**, 3472–3478 (2015).
58. G. Spektor, D. Kilbane, A. K. Mahro, B. Frank, S. Ristok, L. Gal, P. Kahl, D. Podbiel, S. Mathias, H. Giessen, F. J. Meyer Zu Heringdorf, M. Orenstein, M. Aeschlimann, Revealing the subfemtosecond dynamics of orbital angular momentum in nanoplasmonic vortices. *Science.* **355**, 1187–1191 (2017).
59. G. Razinskas, D. Kilbane, P. Melchior, P. Geisler, E. Krauss, S. Mathias, B. Hecht, M. Aeschlimann, Normal-Incidence PEEM Imaging of Propagating Modes in a Plasmonic Nanocircuit. *Nano Lett.* **16**, 6832–6837 (2016).
60. R. G. Ulbrich, G. W. Fehrenbach, Polariton wave packet propagation in the exciton resonance of a semiconductor. *Phys. Rev. Lett.* **43**, 963–966 (1979).
61. K. P. Cheung, D. H. Auston, Excitation of coherent phonon polaritons with femtosecond optical pulses. *Phys. Rev. Lett.* **55**, 2152–2155 (1985).

Acknowledgments: We thank G. Eisenstein, M. Segev, and G. Bartal for the fruitful discussions regarding this manuscript. We thank IDES Ltd and especially S. T. Park for support, advice and discussions. The experiments were performed on the UTEM of the AdQuanta group of I.K., which is installed in the electron microscopy center (MIKA) of the Department of Materials Science and Engineering at the Technion. **Funding:** This project has received funding from the European Union's Horizon 2020 research and innovation programme under grant agreement no. 851780-ERC-NanoEP, the Israel Science Foundation (grant no. 830/19), and the Binational USA-Israel Science Foundation (BSF) 2018288. Y.K. is supported by the Gutwirth and Jacobs Fellowship. hBN crystal growth was supported by National Science Foundation grant CMMI 1538127. **Author contributions:** Y.K and I.K. conceived the project and designed the experiments. R.D. constructed the experimental setup. Y.K., R.D., K.W., M.Y., and Y.A., have conducted the experimental measurements. O.R. developed the theory. Y.K. performed the numerical simulations. Y.K, H.H.S., F.K., M.K., and I.K. wrote the manuscript. L.H.G.T., S.Y.W., M.K. fabricated the first hBN samples and helped in initiating this research, J.L., J.H.E. fabricated the isotopically pure hBN and H.H.S. performed its exfoliation into a TEM membrane. All authors reviewed and discussed the manuscript and made significant contributions to it. **Competing interests:** None declared **Data and materials availability:** All data needed to evaluate the conclusions in the paper are present in the paper or the Supplementary Materials.

Supplementary Materials

Materials and Methods
Supplementary Text
Figs. S1 to S7
Movies S1 to S4
Table S1p